Journal Name

ARTICLE

Bioinspired Sea-sponge Nanostructure Design of Ni/Ni$(HCO_3)_2$-on-C for Supercapacitor with Superior Anti-fading Capacity

Received 00th January 20xx,
Accepted 00th January 20xx

DOI: 10.1039/x0xx00000x

www.rsc.org/

Qingnan Wu, [a, b] Jiahao Wen, [a] Ming Wen, [*a] Qingsheng Wu, [a] and YongQing Fu [c]

Rational design of novel structures plays a key role to achieve high specific capacities and fast charge rates with a long cycling life for battery-type electrodes of supercapacitors. To tackle capacity fading issues of battery-type electrode materials for supercapacitors, a new approach is proposed to form a bioinspired sea-sponge nanostructure of Ni/Ni$(HCO_3)_2$-on-C, synthesized through modifying triangle nanoflakes of Ni$(HCO_3)_2$ with partially *in-situ* reduced Ni generated on sea-sponge-like porous carbon spheres (*S*-PCSs). The conductive skeleton of *S*-PCSs facilitates fast electron transfer and ion diffusion, and maintains the morphology of Ni$(HCO_3)_2$ triangle nanoflakes to ensure a high specific capacity of Ni/Ni$(HCO_3)_2$ nanoflakes. Simultaneously the *in-situ* reduced Ni acts as capacity reservoirs to prevent the fading of the specific capacity. When applied as a positive electrode material, such sea-sponge nanostructures of Ni/Ni$(HCO_3)_2$-on-C exhibit a high specific capacity (472 mAh g^{-1}) with a good rate capability (66% capacity retention at 32 A g^{-1} *vs* 8 A g^{-1}), superior reversibility and cyclability (92% capacity retention after 10,000 cycles). An asymmetric supercapacitor based on Ni/Ni$(HCO_3)_2$-on-C*//S*-PCSs shows a high energy density of 51.3 Wh kg^{-1} at a power density of 4 kW kg^{-1} with a capacitance retention of 89.6% over 6,000 cycles.

1. Introduction

In electrochemical energy storage (EES) systems, supercapacitor becomes one of the key players due to its high power density (>10 kW kg^{-1}), fast charge rate (within seconds) and long cycle life (>100,000 cycles).[1-5] As one type of the key supercapacitors, pseudocapacitor is dependent upon the redox reactions to store the energy, and can generally provide a high energy density.[6-9] However, it often shows a poor cycling life, due to its sluggish reaction kinetics and structural degradations of electrode nanomaterials in the charge-discharge processes.[10-11] Therefore, the power density and cyclability of the pseudocapacitors were often sacrificed in order to increase their energy densities.

To solve the above problems, the pseudocapacitor nanomaterials should have large contact surfaces between electrode and electrolyte, and also stable nanostructures in order to achieve fast electron transfer and short diffusion paths of ions.[12-14] Therefore, various nanomaterials with porous structures have recently been explored for the electrode nanomaterials with high specific capacity and long cycle life.[15-18] Among these, three-dimensional (3D) porous carbon-based nanocomposites have attracted significant attention.[19-26] The porous carbon has good conductivity and relatively large specific surface areas, which can be applied as a frame supporter to disperse active species electrochemically for achieving a high specific capacity.[27,28] The nickel oxygenated chemicals, based on redox reaction mechanisms of Ni(II)/Ni(III) in an alkaline electrolyte, show high values of theoretical capacity, and thus are recently emerged as promising candidates for electrode nanomaterials of pseudocapacitance.[29-31] Among nickel oxygenated chemicals, Ni$(HCO_3)_2$ could provide a relatively higher specific capacity and a better stability according to literature.[32-35] Therefore, carbon-Ni$(HCO_3)_2$ nanocomposites, combining the advantages of conductive porous carbon supporters and high capacity of Ni$(HCO_3)_2$, could attain both high energy density and power density in the supercapacitor. However, currently there are critical problems of quick fading of the specific capacity and short cycle life for the supercapacitors if these carbon-Ni$(HCO_3)_2$ nanocomposites are used as the electrode materials.

In our work, a new architecture of sea-sponge-like Ni/Ni$(HCO_3)_2$-on-C nanocomposite has been designed and synthesized by decorating triangle Ni$(HCO_3)_2$ nanoflakes onto sea-sponge-like porous carbon spheres (*S*-PCSs), followed by partially *in-situ* reduction process. Due to the benefits from the conductive *S*-PCSs and high capacity of Ni$(HCO_3)_2$ with partially *in-situ* reduced Ni as a capacity reservoir, such a sea-sponge-like nanostructure of Ni/Ni$(HCO_3)_2$-on-C can provide short transfer paths for ions and electrons. The *in-situ* produced Ni can be converted into NiOOH in the activation process, which can be served as a capacity reservoir to reinforce the capacity retention of Ni$(HCO_3)_2$ and improve the anti-fading capacity. Therefore, assembling Ni/Ni$(HCO_3)_2$ nanoflakes onto the *S*-PCSs could be an efficient way to ensure high specific

[a] *School of Chemical Science and Engineering, Shanghai Key Laboratory of Chemical Assessment and Sustainability, Tongji University, Shanghai 200092, China.*
[b] *College of Plant Protection, Henan Agricultural University, Zhengzhou 450002, China.*
[c] *Faculty of Engineering and Environment, Northumbria University, Newcastle upon Tyne, NE1 8ST, UK.*
Electronic Supplementary Information (ESI) available. See DOI: 10.1039/x0xx00000x

capacity, good rate capability and long cycling life (92% capacity retention over 10,000 cycles). Furthermore, the superior electrochemical performance of Ni/Ni$(HCO_3)_2$-on-C and *S*-PCSs has a great potential for their practical applications in advanced asymmetric supercapacitors.

2. Experimental details

2.1. Synthesis of Ni/Ni$(HCO_3)_2$-on-C nanocomposite

The typical synthesis process was performed by decorating the triangle Ni$(HCO_3)_2$ nanoflakes onto *S*-PCS, followed by the partially *in-situ* reduction process. The first step was the preparation of Ni$(HCO_3)_2$-on-C nanocomposite. In a typical synthesis experiment, the pretreated *S*-PCS (60 mg) and $Ni(NO_3)_2{\cdot}6H_2O$ (290 mg) were added into a mixed solvent of ethylene glycol and deionized water with a volume ratio of 7:1 and a total volume of 12 mL, and then sonicated (at a frequency of 100 kHz) for 30 min. The urea (240 mg) was added into the above solution under a constant magnetic stirring for 60 min. The mixture was then transferred into a 20 mL Teflon-lined stainless steel autoclave under a temperature of 160℃ for 12 hrs. The collected precipitate product of Ni$(HCO_3)_2$-on-C was washed with deionized water and ethanol in a sequence, and dried in a vacuum oven at 60℃ for overnight. The second step was the formation of sea-sponge-like nanostructures of Ni/Ni$(HCO_3)_2$-on-C, which was followed by an *in-situ* reduction process. $NaHCO_3$ (500 mg) was dissolved into ethylene glycol (15 mL) under a continuous stirring for 60 min, then the prepared Ni$(HCO_3)_2$-on-C was added inside and agitated ultrasonically for 30 min. The mixture was transferred into a 20 mL Teflon-lined stainless steel autoclave heated to 160℃ and maintained for 12 hrs. Finally, the precipitate product of Ni/Ni$(HCO_3)_2$-on-C nanocomposite was obtained, washed with deionized water and ethanol in a sequence, and finally dried at 60℃ in a vacuum oven for overnight.

2.2 Characterization

Morphology and sizes of the products were measured using a field-emission scanning electron microscope (FE-SEM, JEOL, S-4800) and a transmission electron microscope (TEM, JEOL, JEM-2100EX). Elemental analysis was conducted using an energy-dispersive X-ray spectroscope (EDX, Oxford, TN-5400). Crystalline structures of the products were characterized using a powder X-ray diffraction (XRD, Bruker, D8 Advance) with Cu Kα X-ray radiation source (λ=0.154056 nm). The chemical elements and their binding states were analysed using an X-ray photoelectron spectroscope (XPS, Perkin Elmer, PHI-5000C ESCA) with an Al Kα radiation (*hv*=1486.6 eV). The peak shifts of the spectra were calibrated using the surface carbon (C *1s*=284.6 eV) and the data analysis was carried out using the XPSPeak41. Thermal properties of the nanomaterials were characterized using thermogravimetric (TG, Netzsch, STA409PC) and differential scanning calorimeter (DSC, Netzsch, STA409PC) with temperatures from 30 to 800℃ and a heating rate of 10℃ min^{-1} in air. The specific surface areas and pore sizes of the composites were determined based on a Brunauer Emmett Teller method (BET, Micromeritics, ASAP2020) at -196℃.

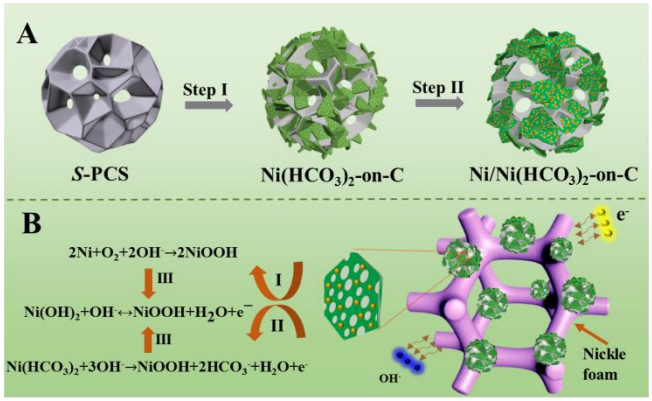

Fig. 1. (A) Fabrication scheme of Ni/Ni$(HCO_3)_2$-on-C nanocomposites. (B) electrochemical storage mechanism of Ni/Ni$(HCO_3)_2$-on-C in three-electrode cell system.

3. Results and discussions

3.1. Formation and electrochemical mechanism

Fig. 1A illustrates the fabrication process of Ni/Ni$(HCO_3)_2$-on-C nanocomposites, which were synthesized through modifying the triangle Ni$(HCO_3)_2$ nanoflakes onto the *S*-PCS followed by partially *in-situ* reduction process. The *S*-PCS with interconnected channels and large specific surface areas was synthesized by ultrasonically spraying pyrolysis, which provides a rigid support to disperse Ni$(HCO_3)_2$.[36,37] During the synthesis process, the OH^- species produced by urea hydrolysis react with Ni^{2+} to form an ultrathin $Ni(OH)_2$ film. The HCO_3^-, generated from CO_2 hydrolysis process, reacts with $Ni(OH)_2$ to form Ni$(HCO_3)_2$ nanoflakes (see Step I in Fig. 1A).[32] The chemical reactions in these processes are summarized as follows:

Urea hydrolysis:

$$CO(NH_2)_2+3H_2O \rightarrow 2NH_3{\cdot}H_2O+CO_2 \quad (1)$$

$$NH_3{\cdot}H_2O \rightarrow NH_4^+ + OH^- \quad (2)$$

Precipitation of ultrathin $Ni(OH)_2$ film:

$$Ni^{2+}+2OH^- \rightarrow Ni(OH)_2 \quad (3)$$

CO_2 hydrolysis:

$$CO_2+H_2O \rightarrow HCO_3^- + H^+ \quad (4)$$

Precipitation of Ni$(HCO_3)_2$ nanoflakes:

$$Ni(OH)_2+2HCO_3^- \rightarrow Ni(HCO_3)_2+2OH^- \quad (5)$$

The morphologies of Ni$(HCO_3)_2$-on-C nanocomposites obtained at different process stages are shown in Fig. S1, confirming the proposed synthesis mechanisms. Afterwards, the partially *in-situ* reduction process of Ni$(HCO_3)_2$-on-C results in the formation of sea-sponge-like Ni/Ni$(HCO_3)_2$-on-C nanocomposite in ethylene glycol, assisted by $NaHCO_3$ to increase the electrode potential of Ni$(HCO_3)_2$ (Fig. 1A, Step II).[38,39] The chemical reactions of *in-situ* reduction process are summarized as follows:

$$Ni(HCO_3)_2+2e^- = Ni+2HCO_3^- \quad (6)$$

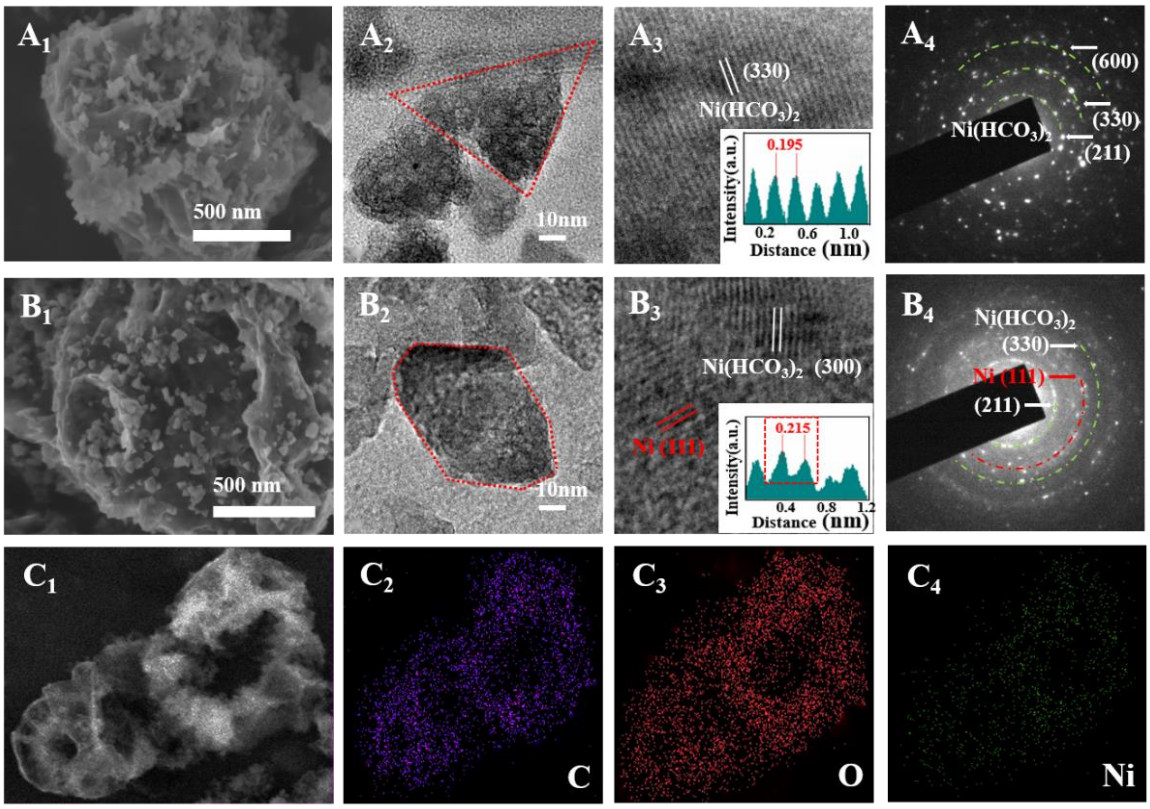

Fig. 2. SEM, TEM, HRTEM images with corresponding SADE patterns of (A) $Ni(HCO_3)_2$-on-C and (B) $Ni/Ni(HCO_3)_2$-on-C. (C) Elemental mapping images of $Ni/Ni(HCO_3)_2$-on-C composite.

$$C_2O_4^{2-}+8H_2O+8e^-=C_2H_6O_2+10OH^- \quad (7)$$

3.2. Morphology and structural analysis

Fig. 2 shows the SEM and TEM images of $Ni(HCO_3)_2$-on-C and $Ni/Ni(HCO_3)_2$-on-C nanocomposites. The triangle $Ni(HCO_3)_2$ nanoflakes (~50 nm) are covered on the surfaces of skeleton structures of *S*-PCS (Fig. $2A_{1,2}$ and Fig. S2B). The *S*-PCSs (~2 μm in diameter, Fig. S3) have interconnected channel structures with a width of ~300 nm as shown in Fig. S2A, which is beneficial for the electrolytic infiltration and ion diffusion in electrochemical reaction process. The SEM image and its corresponding distribution column diagram of *S*-PCS are shown in Fig. S3. In Fig. $2A_3$, the high resolution TEM (HRTEM) image of $Ni(HCO_3)_2$ proves that these triangle nanoflakes are highly crystallized structures with a lattice fringes spacing of 0.195 nm, which corresponds to the (330) plane of $Ni(HCO_3)_2$. The patterns of selected area electron diffraction (SAED) in Fig. $2A_4$ show the polycrystalline diffraction rings for the lattice planes of $Ni(HCO_3)_2$, i.e., (211), (330) and (600). For the $Ni/Ni(HCO_3)_2$-on-C, the shape of $Ni(HCO_3)_2$ nanoflakes is changed from triangle into irregular shape after the partially *in-situ* reduction process (Fig. $2B_{1,2}$, and Fig. S2C). As shown in Fig. $2B_3$, the mixed lattice fringes with a spacing of 0.195 nm and another spacing of 0.215 nm are corresponding to (330) plane of $Ni(HCO_3)_2$ and (111) plane of Ni, indicating co-existence of crystallized metallic Ni inside the $Ni(HCO_3)_2$ nanocrystals. The corresponding SAED patterns show the polycrystalline diffraction rings, corresponding to the lattice planes of (211) and (330) of the $Ni(HCO_3)_2$ and the lattice plane (111) of Ni (Fig. $2B_4$). The nitrogen adsorption-desorption curve exhibits a type IV isotherm for the $Ni/Ni(HCO_3)_2$-on-C nanocomposite (Fig. S4), confirming its mesoporous nanostructures.[32,40] Such nanostructures with numerous interconnected nanopores provide a large specific surface area of 125.2596 $m^2 g^{-1}$ (Table S1), which can significantly enhance the ion diffusion and provide numerous activated sites for the electrochemical reactions. In Fig. 2C, EDX mapping of $Ni/Ni(HCO_3)_2$-on-C confirms that the

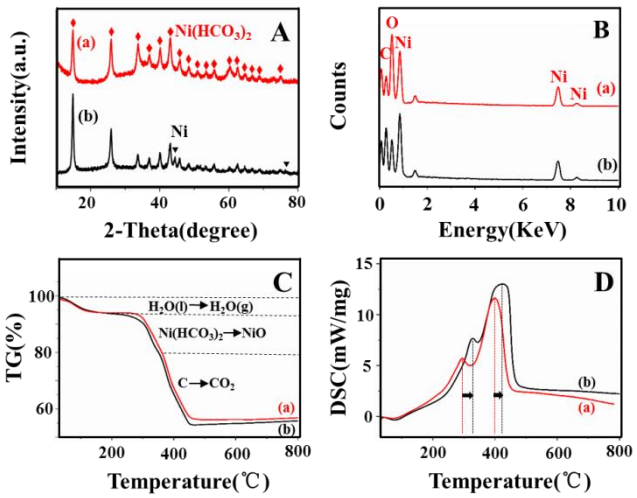

Fig. 3. (A) XRD, (B) EDX, (C) TG and (D) DSC patterns of (a) $Ni(HCO_3)_2$-on-C and (b) $Ni/Ni(HCO_3)_2$-on-C.

Table 1. EDX data of *S*-PCS, $Ni(HCO_3)_2$-on-C and $Ni/Ni(HCO_3)_2$-on-C.

Sample	C (weight%)	O (weight%)	Ni (weight%)
S-PCS	100	-	-
$Ni(HCO_3)_2$-on-C	21.99	31.74	46.27
$Ni/Ni(HCO_3)_2$-on-C	35.83	17.49	46.68

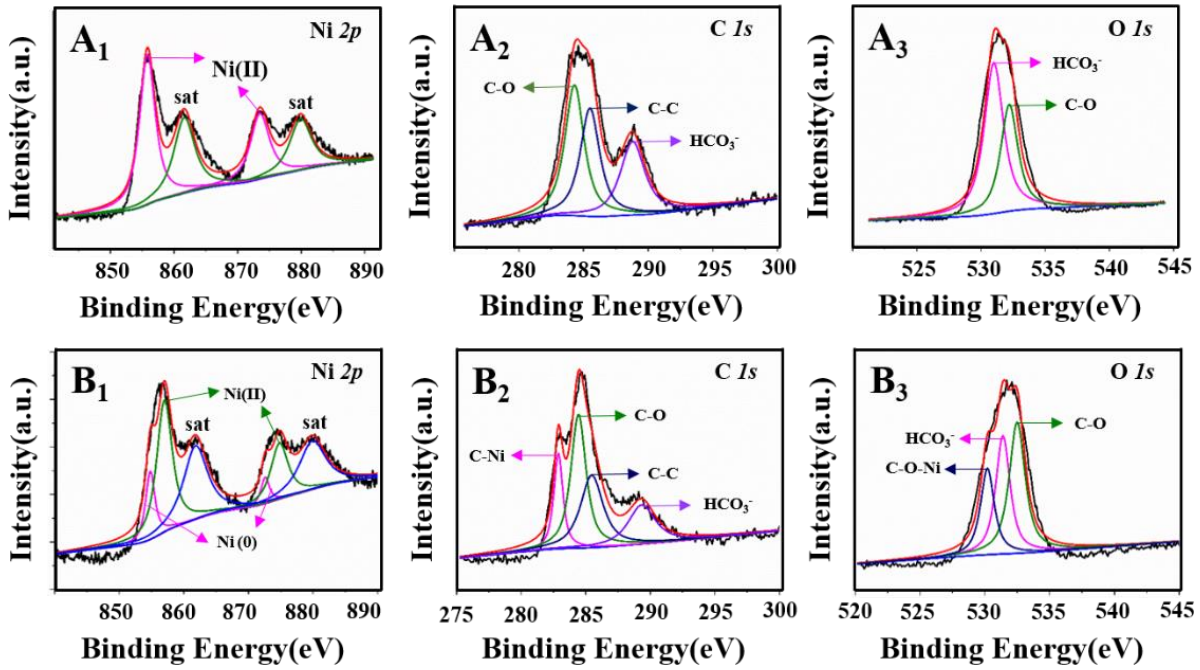

Fig. 4. The high-resolution XPS spectra of (A) $Ni(HCO_3)_2$-on-C and (B) $Ni/Ni(HCO_3)_2$-on-C for Ni *2p*, C *1s*, and O *1s*.

spherical nanostructures are $Ni/Ni(HCO_3)_2$ nanoflakes covered on the surfaces of *S*-PCS. To be compared with, the EDX mapping of *S*-PCS is provided in Fig. S5.

Fig. 3 shows the analysis results of XRD, EDX, TG and DSC for the prepared samples. From the XRD analysis, eighteen explicit peaks can be observed for the $Ni(HCO_3)_2$-on-C, which are all corresponding to the planes of $Ni(HCO_3)_2$ (JCPDS#15-0782). This proves the formation of highly crystallized $Ni(HCO_3)_2$ on *S*-PCS (Fig. 3A). For the $Ni/Ni(HCO_3)_2$-on-C, apart from the peaks of $Ni(HCO_3)_2$-on-C, two extra diffraction peaks at 44.4º (111) and 76.1º (220) can be indexed to the face-centre-cubic (fcc) phase of Ni (JCPDS#65-0380), indicating the success of *in-situ* reduction of $Ni(HCO_3)_2$. The weak diffraction peaks of Ni phase can be observed in the XRD curve, indicating that there is small amount of Ni existed in the

$Ni/Ni(HCO_3)_2$-on-C, which agrees with XPS results. The samples with different Ni contents were prepared and characterized, and the results are shown in Fig. S6. In addition, all the samples show a broad and weak peak at a 2θ of 24°, which is attributed to the amorphous nature of *S*-PCS. Results of XRD, HRTEM and SAED patterns of *S*-PCS are presented in Fig. S7. In Fig. 3B, EDX spectra show the existence of C, O, Ni elements in all the samples. Although the weight percentage of Ni did not show apparent changes after the partially *in-situ* reduction process, the weight percentage of oxygen was found to decrease and the weight percentage of carbon to increase (as listed in Table 1). These prove the formation of mixed nanostructure of $Ni/Ni(HCO_3)_2$, which is in a good agreement with the XRD results. The TG results are shown in Fig. 3C. All these curves could be divided into three stages: e. g., solvent evaporation (below 100℃); decomposition of $Ni(HCO_3)_2$ (280℃~350℃); and decomposition of *S*-PCS (350℃~450℃), respectively. Based on the measured weight losses, the weight percentages of $Ni/Ni(HCO_3)_2$ and S-PCS for the $Ni/Ni(HCO_3)_2$-on-C nanocomposites were calculated to be ~70% and ~25%. In Fig. 3D, DSC measurements show that the transition temperatures of $Ni/Ni(HCO_3)_2$-on-C at different stages are higher than those of $Ni(HCO_3)_2$-on-C, mainly due to the formation of new bonds in the $Ni/Ni(HCO_3)_2$-on-C (such as C-O-Ni and C-Ni) between *S*-PCS and $Ni/Ni(HCO_3)_2$ during the *in-situ* reduction process. To be compared with, the EDX pattern and TG spectrum of *S*-PCS are given in Fig. S5.

XPS analysis was performed to confirm the formation of new chemical bonds (Fig. S8). The photoemission peaks of Ni *2p*, C *1s* and O *1s* appear in the survey scan spectra of both the $Ni(HCO_3)_2$-on-C and $Ni/Ni(HCO_3)_2$-on-C. For the $Ni(HCO_3)_2$-on-C, the high resolution spectrum of Ni *2p* exhibits two peaks at 855.8 eV and 873.5 eV along with their corresponding satellite peaks at 861.6 eV and 879.9 eV, indicating the existence of Ni^{2+} in $Ni(HCO_3)_2$-on-C (Fig. $4A_1$). In the high resolution spectrum of C *1s*, the photoemission peak can be deconvoluted into three peaks at 284.3 eV, 285.5 eV

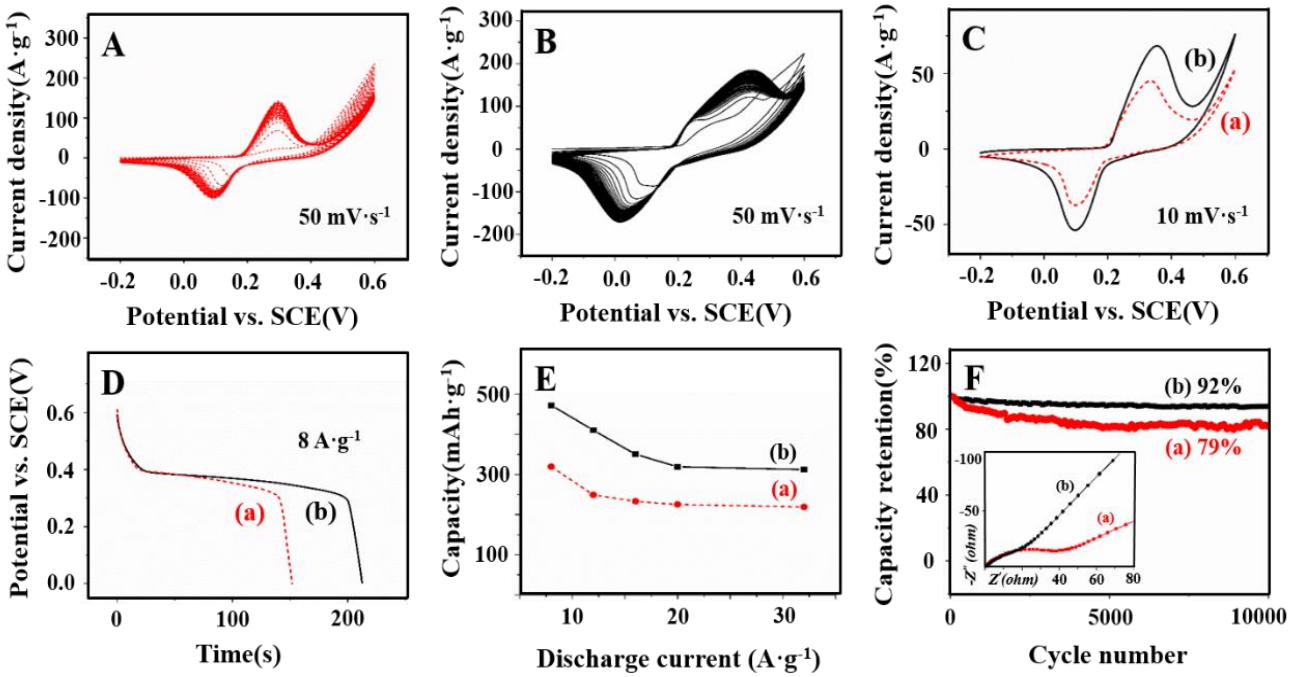

Fig. 5. The electrochemical performance of (a) $Ni(HCO_3)_2$-on-C and (b) $Ni/Ni(HCO_3)_2$ on-C: (A, B) The activation processes. (C) CV curves. (D) Discharge curves. (E) The capacities at different current densities calculated by discharging curves. (F) The cycle performances at a current density of 10 A g^{-1} with an inset of Nyquist plots.

and 288.8 eV, respectively, corresponding to the chemical bonds of C-O and C-C in *S*-PCS and HCO_3^- in triangle $Ni(HCO_3)_2$ nanoflakes (Fig. $4A_2$). As shown in Fig. $4A_3$, the O *1s* peak can be deconvoluted into two peaks at 531.7 eV and 532.5 eV, which are assigned to the bonds of HCO_3^- and C-OH, proving that the $Ni(HCO_3)_2$ nanoflakes are covered on the *S*-PCS surfaces. For the $Ni/Ni(HCO_3)_2$-on-C, the peaks of Ni $2p_{3/2}$ and Ni $2p_{1/2}$ can be deconvoluted into four peaks at 854.7 eV and 872.5 eV, 855.8 eV and 873.5 eV, which are assigned to Ni^0 in metallic Ni and Ni^{2+} in $Ni(HCO_3)_2$, indicating the formation of $Ni/Ni(HCO_3)_2$ composites (Fig. $4B_1$). To further verify the existence of metallic Ni^0 in $Ni/Ni(HCO_3)_2$-on-C, the raw data of Ni *2p* spectra for both $Ni/Ni(HCO_3)_2$-on-C and $Ni(HCO_3)_2$-on-C were analysed and the results are shown in Fig. S8. According to these curves, an obvious shift appeared in the $Ni/Ni(HCO_3)_2$-on-C reveals its lower energy in $Ni/Ni(HCO_3)_2$-on-C products. The reason is that the metallic Ni has a lower binding energy, indicating the existence of metallic Ni in $Ni/Ni(HCO_3)_2$-on-C. In Figs. $4B_2$ and $4B_3$, apart from the peaks which are already presented in those of $Ni(HCO_3)_2$-on-C, there are new bonds of C-Ni at 283.6 eV and C-O-Ni at 530.2 eV obtained after the partially *in-situ* reduction process,[11] which can well-explain the results from the TG measurement. These new bonds play important roles in the electrochemical processes. They not only enhance the binding forces among different components, but also stabilize the nanostructures during charge-discharge

processes. They can also significantly improve the electrical conductivity and promote the ion diffusion and electron transfer.

3.3. Electrochemical characterization of nanocomposites

Electrochemical performance of both the $Ni(HCO_3)_2$-on-C and $Ni/Ni(HCO_3)_2$-on-C was measured based on a three-electrode cell system. The increasing cyclic voltammetry (CV) areas in Figs. 5A and 5B show the electrochemical activation processes of as-obtained samples, which are mainly contributed from $Ni(HCO_3)_2$ and $Ni/Ni(HCO_3)_2$. This process is presented in Fig. S9.[41-43] Typical CV curves of samples at the same scan rate (10 mV s^{-1}) were obtained and the data are summarized in Fig. 5C. In these CV curves, pairs of redox couple peaks can be observed, which are linked with the fast and reversible reactions of Ni^{3+}/Ni^{2+} redox couples, proving their suitability as the battery-type electrode nanomaterial. However, it is observed that the CV area and peak current density of the $Ni/Ni(HCO_3)_2$-on-C are apparently larger than those of the $Ni(HCO_3)_2$-on-C, indicating a larger specific capacity of the $Ni/Ni(HCO_3)_2$-on-C. Fig. 5D shows discharge curves of these two samples operated at the same current density (8 A g^{-1}). According to the computational formula, the specific capacity is positively correlated to the discharge time, which demonstrates a good consistency with the results displayed in the CV curves. The CV and galvanostatic charging-discharging (GCD) curves of as-prepared samples at different scan rates or current densities, as well as the corresponding specific capacitances were further investigated (Fig. S10, S11 and S12). The specific capacities obtained from the different discharging curves are summarized in Fig. 5E. It should be noted that the specific capacity is negatively correlated to the current density, mainly because the kinetics of redox reactions are too slow to follow the potential changes. As shown in the graph, the $Ni/Ni(HCO_3)_2$-on-C exhibits a larger specific capacity (472 mAh g^{-1}) than that of $Ni(HCO_3)_2$-on-C (249 mAh g^{-1}) at a current density of 8 A

Table 2 Cycling life of various Ni-based electrode nanomaterials reported in the literature.

Materials	Specific capacitance	Cycling life	Ref. (year)
Manganese carbonate quantum dots/$Ni(HCO_3)_2$-$MnCO_3$	2641.3 F g^{-1} at 3 A g^{-1}	91.3% (10,000)	44(2015)
3D porous $Ni(OH)_2$	2110 F g^{-1} at 1 A g^{-1}	53% (2,000)	45(2018)
Ultrathin $NiCo_2S_4$@graphene	1432 F g^{-1} at 1 A g^{-1}	84.3% (5,000)	46(2018)
Ni-Co hydroxide embedded in GH	544 C g^{-1} at 2 A g^{-1}	85% (5,000)	47(2018)
$NiCo_2S_4$/graphene	1063 F g^{-1} at 2 A g^{-1}	82% (10,000)	48(2018)
Ni-EA (ellagic acid)	1050 F g^{-1} at 0.5 A g^{-1}	91.8% (4,000)	49(2018)
$Ni/Ni(HCO_3)_2$-on-C	2888 F g^{-1} at 8 A g^{-1}	92% (10,000)	This work

Table 3 Energy densities and power densities of various supercapacitors based on carbon/Ni-compound as positive electrode nanomaterials reported in the literature.

Materials	Energy density (Wh kg^{-1})	Power density (kW kg^{-1})	Ref.(year)
PNTs[(a)]@$NiCo_2S_4$//PNTs@$NiCo_2S_4$	21.3	0.417	51 (2017)
Co_3O_4@$NiCo_2O_4$//AC	75.6	1.053	52 (2017)
Ni–P@Ni–Co//AC[(b)]	28.9	0.4	53 (2018)
$NiCo_2O_4$–PPy[(c)]//AC	45.6	0.362	54 (2018)
Ppy@$NiCo_2S_4$//N-C[(d)]	50.82	0.16	55 (2018)
P doped $Ni(OH)_2$//AC	81.3	0.635	56 (2018)
CoP@$Ni(OH)_2$//AC	89.6	0.91	57 (2018)
$Ni/Ni(HCO_3)_2$-on-C//*S*-PCS	51.3	4	This work

[(a)] shorted for polyporrole nanotubes. [(b)] shorted for active carbon; [(c)] shorted for polypyrrole; [(d)] shorted for nitrogen-doped carbon nanotubes;

Fig. 6. Electrochemical characteristics of $Ni/Ni(HCO_3)_2$-on-C//*S*-PCSs. (A) Electrochemical storage mechanism. (B) Cycle performances, inset with the photograph of hybrid supercapacitor powering one light-emitting diode. (C) Ragone plots.

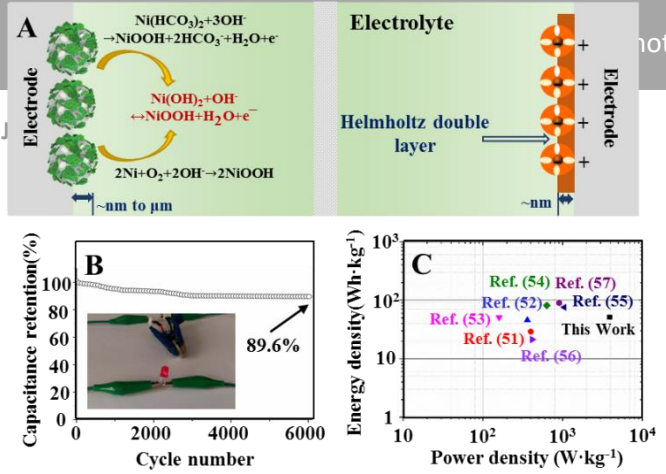

g^{-1}, and its specific capacity can still be maintained at 66% at a current density of 32 A g^{-1}, compared with that at 8 A g^{-1}, indicating its high rate capability.

Cycle life is one of important parameters for evaluating the nanocomposite to be used as an electrode material, thus the prepared samples were tested at a current density of 10 A g^{-1} in this study (Fig. 5F). For both two curves, the capacity retentions have not shown any apparent decrease in the initial stage. For the $Ni(HCO_3)_2$-on-C, it has a 21% decrease after 10,000 cycles, mainly owing to the poor electrical conductivity and slow reaction kinetics of Ni-based nanomaterial in redox reactions. However, the capacity of the $Ni/Ni(HCO_3)_2$-on-C has hardly showed apparent changes and could maintain 92% even after 10,000 cycles, which is mainly attributed to the formation of capacity reservoirs due to the metallic Ni. Moreover, SEM and TEM images of $Ni/Ni(HCO_3)_2$-on-C before and after cycles have been taken (Fig. S13). The $Ni/Ni(HCO_3)_2$ nanostructures covered on the S-PCS show minor agglomeration after cycling, but the 3D *S*-PCS backbone maintains the same morphological characteristics with the previous ones, indicating the stability of this nanostructure. Furthermore, the electrical conductivities of the *S*-PCS, $Ni(HCO_3)_2$-on-C and $Ni/Ni(HCO_3)_2$-on-C were characterized using the electrochemical impedance spectroscopy (EIS, see Fig. 5F Inset and Fig. S14). The smaller Rct value for the $Ni/Ni(HCO_3)_2$-on-C indicates a lower charge-transfer resistance at the interfaces between the electrode and electrolyte. The slope of a linear line at the lower frequency region, ascribed to the Warburg impedance, demonstrates a faster rate of ion diffusion at the interfaces between electrolyte and electrode for the $Ni/Ni(HCO_3)_2$-on-C than that of the $Ni(HCO_3)_2$-on-C. The electrochemical performance of $Ni/Ni(HCO_3)_2$-on-C, which excels at high capacity and has a good cycling capability, is superior to most recently reported carbon/Ni compound materials, as summarized in Table 2.[44-49]

3.4. Electrochemical performances of $Ni/Ni(HCO_3)_2$-on-C//*S*-PCS supercapacitor

An asymmetric supercapacitor based on $Ni/Ni(HCO_3)_2$-on-C//*S*-PCS was fabricated and measured in an aqueous electrolyte of 6 M KOH. The electrochemical mechanisms of positive and negative electrode nanomaterials are exhibited in Fig. 1B and Fig. 6A, which are attributed to Faradic redox reactions and electrostatic accumulation of surface charges, respectively.[50] To obtain the best electrochemical performance, the mass loadings between the two electrodes were calculated according to a charge balance theory.[11] The detailed electrochemical results of both the $Ni/Ni(HCO_3)_2$-on-C and *S*-PCS are shown in Fig. S10 and S15, respectively. Unlike the symmetrically rectangular shaped CV curves commonly observed in most of carbon materials, the CV curves of *S*-PCS exhibit a pair of weak redox peaks. This indicates that the capacitance is partially generated by the Faradic redox reactions, due to the oxygen functional groups in the *S*-PCS composite (Fig. S7). In Fig. S16A, the CV curves of the as-fabricated supercapacitor display a rectangle shape together with a pair of weak redox peaks, indicating the existence of hybrid capacitive behaviours of *S*-PCS (non-Faradaic) and $Ni/Ni(HCO_3)_2$-on-C (Faradaic). Meanwhile, the GCD curves in Fig. S16B show a nearly linear behaviour in the discharge stages, indicating a capacitor-like behaviour of $Ni/Ni(HCO_3)_2$-on-C//*S*-PCS. The specific capacitance of this asymmetric capacitor, calculated based on the total mass of active materials, reaches a maximum value of 144.4 F g^{-1} at a current density of 5 A g^{-1}.

Fig. 6B shows the cycling performance of this fabricated asymmetric capacitor based on GCD curves at a current density of 10 A g^{-1}. After 6,000 cycles, the capacitance retention is still 89.6%, indicating a good cycling stability of this asymmetric capacitor. Furthermore, it was used to power a light emitting diode (1.5 V) to show its capability, and the result is shown in inset of Fig. 6B. In addition, the energy storage performance of the $Ni/Ni(HCO_3)_2$-on-C//*S*-PCS asymmetric supercapacitor was evaluated using the Ragone plot (i.e., the relationship between energy density and power density), and the results are shown in Fig. 6C. It can reach a maximum energy density of 51.3 Wh kg^{-1} at a power density of 4 kW kg^{-1}, which is much higher than many of those reported in literature for the hybrid supercapacitors as summarized in Table 3.[51-57] These results clearly demonstrate the high-performance of $Ni/Ni(HCO_3)_2$-on-C//*S*-PCS asymmetric supercapacitor, indicating its potential practically applications.

4. Conclusions

In conclusion, a novel sea-sponge nanostructure of $Ni/Ni(HCO_3)_2$-on-C has been successfully prepared using a 3D matrix of *S*-PCS to disperse and support triangle $Ni(HCO_3)_2$ nanoflakes followed by partially *in-situ* reduction process to form metallic nanostructured Ni. The 3D-structured conductive *S*-PCS with large specific surface areas ensures the stability of $Ni/Ni(HCO_3)_2$-on-C in electrochemical reactions, and enable a high specific capacity and a much improved cycle life with 92% capacity retention over 10,000 cycles at a current density of 10 A g^{-1}. The as-fabricated $Ni/Ni(HCO_3)_2$-on-C//*S*-PCS asymmetric supercapacitor showed a power density of 4 kW kg^{-1} at an energy density of 51.3 Wh kg^{-1} with a capacitance retention of 89.6% over 6,000 cycles. The bioinspired sea-sponge nanostructure has been proved as a good electrode material for the high-performances supercapacitors.

Conflicts of interest

There are no conflicts to declare

Acknowledgements

This work was financially supported by the National Natural Science Foundation of China (NSFC Nos: 21171130, 51271132, 51072134 and 91122025), and 973 Project of China (No: 2011CB932404), UK

Engineering and Physical Sciences Research (EPSRC, EP/P018998/1), Newton Mobility Grant (IE161019) through Royal Society.

References

[1] B.E. Conway, Electrochemical Supercapacitors: Scientific Fundamentals and Technological Applications. Boston: Springer US, 1999.

[2] C. Largeot, C. Portet, J. Chmiola, P.L. Taberna, Y. Gogotsi and P. Simon, *J. Am. Chem. Soc.*, 2008, **130**, 2730.

[3] S.G. Kandalkar, D.S. Dhawale, C.K. Kim and C.D. Lokhande, *Synth. Met.*, 2010, **160**, 1299.

[4] A.G. Pandolfo and A.F. Hollenkamp, *J. Power Sources*, 2006, **157**, 11.

[5] V. Augustyn, P. Simon and B. Dunn, *Energy Environ. Sci.*, 2014, **7**, 1597.

[6] E. Faggioli, P. Rena, V. Danel, X. Andrieu, R. Mallant and H. Kahlen, *J. Power Sources*, 1999, **84**, 261.

[7] A.S. Arico, P. Bruce, B. Scrosati and J.M. Tarascon, *Nat. Mater.*, 2005, **4**, 366.

[8] Z.S. Wu, G.M. Zhou, L.C. Yin, W.C. Ren, F. Li and H.M. Cheng, *Nano Energy*, 2012, **1**, 107.

[9] J. Yan, Q. Wang, T. Wei and Z.J. Fan, *Adv. Energy Mater.*, 2014, **4**, 1300816.

[10] Z. Wu, X.L. Huang, Z.L. Wang, J.J. Xu and H.G. Wang, *Sci. Rep.*, 2014, **4**, 3669.

[11] S.P. Chen, Q.N. Wu, M. Wen, C.X. Wang, Q.S. Wu and J.H. Wen, *J. Phys. Chem. C*, 2017, **121**, 9719.

[12] L. Zhang, X. Yang, F. Zhang, G.K. Long, T.F. Zhang and K. Leng, *J. Am. Chem. Soc.*, 2013, **135**, 5921.

[13] L. Wei, M. Sevilla, A.B. Fuertes, R. Mokaya and G. Yushin, *Adv. Energy Mater.*, 2011, **1**, 356.

[14] N. Jha, P. Ramesh, E. Bekyarova, M.E. Itkis and R.C. Haddon, *Adv. Energy Mater.*, 2012, **2**, 438.

[15] J. Yan, Z.J. Fan, W. Sun, G.Q. Ning, T. Wei and Q. Zhang, *Adv. Funct. Mater.*, 2012, **22**, 2632.

[16] J. Chen, H.M. Wei, N. Fu, H.J. Chen, G.X. Lan and H.L. Lin, *J. Mater. Sci.*, 2018, **53**, 2137.

[17] J.G. Wang, H.Z. Liu, H.H. Sun, W. Hua, H.W. Wang and X.R. Liu, *Carbon*, 2018, **127**, 85.

[18] Z.S. Wu, Y. Sun, Y.Z. Tan, S.B. Yang, X.L. Feng and K. Müllen, *J. Am. Chem. Soc.*, 2012, **134**, 19532.

[19] W. Yang, W. Yang, L.N. Kong, A.L. Song, X.J. Qin and G.J. Shao, *Carbon*, 2018, **127**, 557.

[20] X.H. Cao, Y.M. Shi, W.H. Shi, G. Lu, X. Huang and Q.Y. Yan, *Small*, 2011, **7**, 3163.

[21] X.C. Dong, H. Xu, X.W. Wang, Y.X. Huang, M.B. Chan-Park and H. Zhang, *ACS Nano*, 2012, **6**, 3206.

[22] Z.N. Li, S. Gadipelli, Y.C. Yang and Z.X. Guo, *Small*, 2017, **13**, 1702474.

[23] L.F. Chen, Y. Feng, H.W. Liang, Z.Y. Wu and S.H. Yu, *Adv. Energy Mater.*, 2017, **7**, 1700826.

[24] J.F. Ni and Y. Li, *Adv. Energy Mater.*, 2016, **6**, 1600278.

[25] S.Q. Chen, X.D. Huang, H. Liu, B. Sun, W.K. Yeoh and K.F. Li, *Adv. Energy Mater.*, 2014, **8**, 1301761.

[26] S. Rehman, X.X. Gu, K. Khan, N. Mahmood, W.L. Yang and X.X. Huang, *Adv. Energy Mater.*, 2016, **6**, 1502518.

[27] H. Jiang, P.S. Lee and C.Z. Li, *Energy Environ. Sci.*, 2013, **6**, 41.

[28] S.E. Skrabalak and K.S. Sulick, *J. Am. Chem. Soc.*, 2006, **128**, 12642.

[29] J.Y. Ji, L.L. Zhang, H.X. Ji, Y. Li, X. Zhao and X. Bai, *ACS Nano*, 2013, **7**, 6237.

[30] B. Saravanakumar, S.S. Jayaseelan, M.K. Seo, H.Y. Kim and B.S. Kim, *Nanoscale*, 2017, **9**, 18819.

[31] H. Fang, J.F. Yang, M. Wen and Q.S. Wu, *Adv. Mater.*, 2018, **30**, 1705698.

[32] X.X. Zang, Z.Y. Dai, J. Guo, Q.C. Dong, J. Yang and W. Huang, *Nano Res.*, 2016, **9**, 1358.

[33] J.F. Sun, Z.P. Li, J.Q. Wang, Z.F. Wang, L.Y. Niu and P.W. Gong, *J. Alloys Compd.*, 2013, **581**, 217.

[34] Q.X. Xia, K.S. Hui, K.N. Hui, S.D. Kim, J.H. Lim and S.Y. Choic, *J. Mater. Chem. A*, 2015, **3**, 22102.

[35] Y.N. Yan, G. Cheng, P. Wang, D.N. He and R. Chen, *RSC Adv.*, 2014, **4**, 49303.

[36] S. P Chen, Q. N. Wu, Y. F. Fan, M. Wen, Q. S. Wu, Y. Cui, N. Pinna, *ACS Applied Materials & Interfaces*, 2018, **10**, 19656.

[37] S. P. Chen, K. Xing, J. H. Wen, M. Wen, Q. S. Wu, *J. Mater. Chem. A*, 2018, **6**, 7631.

[38] Y. Kuang, G. Feng, P.S. Li, Y.M. Bi, Y.P. Li and X.M. Sun, *Angew. Chem. Int. Ed.*, 2016, **55**, 693.

[39] M. Z. Cheng, M. Wen, S. Q. Zhou, Q. S. Wu and B. L. Sun, *Inorganic Chemistry*, 2012, **51**, 1495.

[40] P. Sennu, M. Christy, V. Aravindan, Y.G. Lee, K.S. Nahm and Y.S. Lee, *Chem. Mater.*, 2015, **16**, 5726.

[41] S. L. Yau, F. R. Fan, T. P, Moffat and A. J. Bard, *J. Phys. Chem.* 1994, **98**, 5493.

[42] A. S. Adekunle and K. L. Ozoemena, *Electrochimica Acta*, 2008, **53**, 5774.

[43] J. Jiang, J. P. Liu, W. W. Zhou, J. H. Zhu, X. T. Huang, X. Y. Qi, H. Zhang and T. Yu, *Energy Environ. Sci.*, 2011, **4**, 5000

[44] Q. X. Xia, K. S. Hui, K. N. Hui, H. Kim, *J. Mater. Chem. A*, 2015, **3**, 22102.

[45] F. Y. Liu, X. Chu, H. Zhang, B. Zhang, W. Q. Yang, *Electrochimica Acta,* 2018, DOI: 10.1016/j.electacta.2018.02.130.

[46] F. Yu, Z. Chang, X. H. Yuan, H. X. Wang, Y. P. Wu, *J. Mater. Chem. A,* 2018, DOI:10.1039/C8TA00835C.

[47] M. Hwang, J. Kang, K. D. Seong, D. K. Kim, X. Z. Jin, W. H. Antink, C. Lee, Y. Z. Piao, *Electrochimica Acta*, 2018, **270**, 156.

[48] X. Yang, H. Liu, H. Jiang, Z. Q. Sun, Q. Wang, F. Y. Qu, *ChemElectroChem*, 2018, DOI:10.1002/celc.201800302

[49] J. X. Gou, S. L. Xie and C. G. Liu, *New J. Chem.*, 2018, DOI: 10.1039/C7NJ04663D.

[50] G.P. Wang, L. Zhang and J.J. Zhang, *Chem. Soc. Rev.*, 2012, **18**, 797.

[51] J. Zhang, H.J. Guan, Y. Liu, Y.F. Zhao and B. Zhang, *Electrochim. Acta*, 2017, **258**, 182.

[52] Y. Lu, L. Li, D. Chen and G.Z. Shen, *J. Mater. Chem. A*, 2017, **5**, 24981.

[53] D.D. Li, Y. Li, Z.Y. Xu, D.W. Wang, T.P. Wang and J. Zhao, *J. Mater. Sci.*, 2018, **53**, 3647.

[54] S. Liu, C.H. An, X.Y. Chang, H.N. Guo, L. Zang and Y.J. Wang, *J. Mater. Sci.*, 2018, **53**, 2658.

[55] Y.Y. Zheng, J. Xu, X.S. Yang, Y.J. Zhang, Y.Y. Shang and X.Y. Hu, *Chem. Eng. J.*, 2018, **333**, 111.

[56] K.Z. Li, S.K. Li, F.Z. Huang, Y. Lu, L. Wang and H. Chen, *Appl. Surf. Sci.*, 2018, **428**, 250.
[57] J. Wen, S. Li, T. Chen, B. Li, L. X iong and Y. Guo, Electrochim. Acta, 2017, **258**, 266.